GEOPHYSICS, VOL. 80, NO. 2 (MARCH-APRIL 2015); P. IM21–IM33, 9 FIGS.
10.1190/GEO2014-0212.1

Horizon volumes with interpreted constraints

Xinming Wu[1] and Dave Hale[1]

ABSTRACT

Horizons are geologically significant surfaces that can be extracted from seismic images. Color coding of horizons based on amplitude or other attributes can help reveal ancient sedimentary environments and structural features. Extracted horizons are also used for building structure models and stratigraphic interpretations. We propose two methods for constructing seismic horizons aligned with reflectors in a 3D seismic image. The first method generates horizons one at a time; the second method generates an entire volume of horizons at once by first computing a relative geologic time volume from seismic normal vectors. Rather than gradually building a horizon by extending one or more seed points to a surface along seismic reflectors, both of our methods generate whole horizons at once by solving partial differential equations derived from seismic normal vectors. The most significant new aspect of both methods is the ability to specify, perhaps interactively during interpretation, a small number of control points that may be scattered throughout a 3D seismic image. Experiments revealed that with our method, control points enable the extraction of more accurate horizons from seismic images in which noise, unconformities, and faults are apparent. These points represent constraints that we implemented as preconditioners in the conjugate gradient method used to construct horizons.

INTRODUCTION

In seismic interpretation, by visually tracking or automatically extracting surfaces throughout a 3D seismic image along consistent seismic waveforms, such as peaks, troughs, or zero-crossing points, and to a lesser extent, relatively constant phase, we are able to identify seismic horizons. These horizons are assumed to correspond to stratal surfaces, which are primary beddings or ancient depositional surfaces that are geologically synchronous (Vail et al., 1977). Color coding of horizons based on amplitude or other attributes can help reveal ancient depositional environments and geomorphic features (Posamentier et al., 2007). Therefore, extracting horizons from seismic images is a common and important problem for seismic interpretation.

Horizon volume

Zeng et al. (1998b) present the concept of a *stratal time model* and generate such a model with a limited number of interpreted horizons and therefore with limited resolution. A *horizon cube* (de Groot et al., 2010; Qayyum et al., 2012) is a volume containing a dense set of stratigraphic surfaces (Brouwer et al., 2011), which is similar to a stratal time model if the surfaces are displayed in the geologic time and space domain. Clark et al. (2010a, 2010b) generate a high-resolution stratal time model, but they called it a *horizon volume*, by using seismic dips estimated from a seismic image. We also prefer to use the term horizon volume instead of stratal time model because we also compute a high-resolution result (Figure 1c) from a high-resolution relative geologic time (RGT) volume (Figure 1b). The RGT volume is computed from seismic normal vectors, which are, similar to seismic dips, estimated from a seismic image (Figure 1a). A horizon volume $t(x, y, \tau)$ (Figure 1c) contains the seismic traveltime location t of horizons as a function of RGT τ and horizontal spatial coordinates x and y. Therefore, a horizon volume (Figure 1c) can be used to flatten reflectors (Figure 1d) or to access all horizons at once. Horizontally slicing a horizon volume yields a traveltime structure map of a horizon corresponding to a constant RGT τ. The concept of an "RGT volume," first presented by Stark (2003, 2004, 2005), is closely related to the horizon volume. An RGT volume $\tau(x, y, t)$ (Figure 1b) contains RGT τ as a function of spatial coordinates x, y, and seismic traveltime t. A surface of constant τ in an RGT volume corresponds to a seismic horizon (Stark, 2003, 2005). The only difference between an RGT volume (Figure 1b) and its corresponding seismic image is that the value of a sample in an RGT volume

Manuscript received by the Editor 6 May 2014; revised manuscript received 27 August 2014; published online 2 February 2015.
[1]Colorado School of Mines, Golden, Colorado, USA. E-mail: xinwu@mines.edu; dhale@mines.edu.

represents geologic time rather than seismic amplitude (Stark, 2005). Given an RGT volume $\tau(x, y, t)$ with τ monotonically increasing with vertical traveltime t, a horizon volume $t(x, y, \tau)$ can be easily obtained via an inverse linear interpolation method (Parks, 2010) or by a time-warping technique (Burnett and Fomel, 2009). In practice, we use both the horizon and RGT volumes to conveniently access horizons. An RGT volume, with axes identical to a seismic image, is first used to look up the RGT value τ for a horizon we wish to extract. A horizon volume is then used to directly obtain the spatial coordinates for the horizon by horizontally slicing the horizon volume for that τ. As we compute an RGT value for every seismic sample, we can extract a horizon at each sample in a seismic image, and therefore obtain all seismic horizons represented in a seismic image.

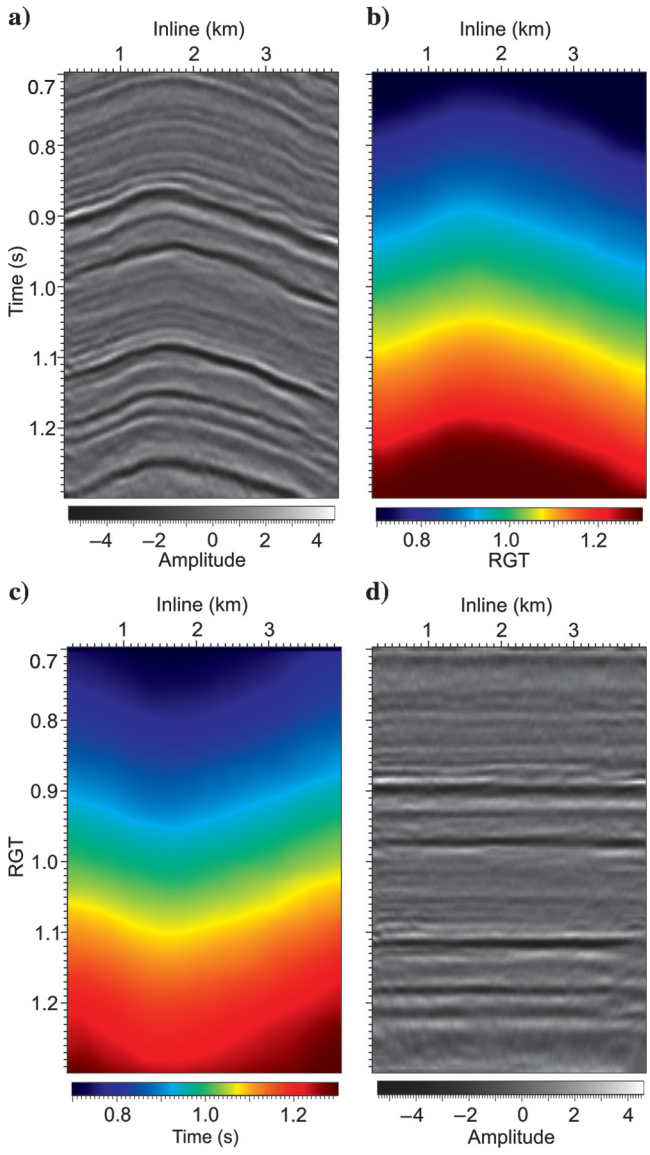

Figure 1. From (a) a seismic image, (b) an RGT volume is computed and then converted to (c) a horizon volume that maps the seismic image to (d) a flattened image.

Previous methods

Methods for obtaining a horizon volume can be generally classified into three categories: The first is stratal slicing (Zeng et al., 1998a, 1998b), which uses several reference horizons to interpolate a stratal time model or horizon volume. With a limited number of horizons for control, the interpolated horizon volume can follow large-scale features but usually cannot resolve local features (Lomask et al., 2011). The second category of methods uses seismic reflector dips (Lomask et al., 2006; Fomel, 2010; Parks, 2010; Karimi and Fomel, 2011) or, similarly, seismic normal vectors, computed for every image sample to be perpendicular to seismic amplitude reflectors. In these methods, a horizon volume is explicitly (Lomask et al., 2006) or implicitly (Fomel, 2010; Parks, 2010; Karimi and Fomel, 2011; Luo and Hale, 2012) generated to map a seismic image from the traveltime-space domain to a flattened image in the RGT-space domain. Horizon volumes generated by these methods are more accurate for revealing local features than those interpolated from several horizons using the first category of methods. The third category is similar to the second one in that these methods also compute high-resolution horizon volumes, but without the use of dips or normal vectors. Instead, they use an RGT volume generated by unwrapping a corresponding seismic instantaneous phase image (Stark, 2003, 2004, 2005; Wu and Zhong, 2012b).

Proposed methods

We first describe a method for extracting single horizons, one at a time, by using precomputed seismic normal vectors, which are perpendicular to seismic amplitude reflectors. This method requires at least one control point to indicate the horizon (containing this point) that we want to extract and to initialize a horizontal surface passing through this point. The initial surface is typically inconsistent with the desired horizon, but it is iteratively deformed until vectors normal to the surface are aligned with vectors normal to a reflector in the seismic image. We extend this method to permit additional control points, which enable reliable extraction of a sequence boundary or a horizon complicated by faults or noise. We then introduce a second method that generates a complete horizon volume constrained by one or more sets of control points, where each set contains more than one control points. To generate a horizon volume (Figure 1c), we first use seismic normal vectors to compute an RGT volume (Figure 1b), from which a horizon volume is then interpolated. This process is similar to Parks's (2010) method for flattening a seismic image, but we instead derive the method in a simpler way. Furthermore, similar to the way in which we extract a more accurate single horizon using control points, we use multiple sets of control points to generate a more accurate horizon volume from a seismic image complicated by faults or noise. Each set of control points belongs to a single horizon with an unspecified RGT value and is easily specified by selecting points that we want to lie on the same horizon. We implement these constraints with simple preconditioners in the conjugate gradient (CG) algorithm that we use to compute the RGT and horizon volumes.

EXTRACTING A SINGLE HORIZON

To extract or construct a single horizon from a 3D seismic image, one usually first picks a reference point or seed. This seed then

grows to a horizon surface by manually or automatically tracking seismic reflectors along seismic amplitude peaks or troughs. Here, we describe a different method that uses at least one control point to initialize a complete horizontal surface and then updates that surface to conform to seismic normal vectors. We then extend this method to enable use of multiple control points, which improve the accuracy and efficiency of horizon extraction.

Horizon extraction without constraints

We first use structure tensors (Van Vliet and Verbeek, 1995; Fehmers and Höcker, 2003) to compute, for each image sample, a unit (or seismic normal) vector $\mathbf{n} = [n_x, \quad n_y, \quad n_t]^\top$ that is perpendicular to the seismic amplitude reflector at that sample location. We notate the unit vectors by time in the vertical dimension, but we consider a seismic image by samples in horizontal and vertical dimensions when we estimate those normal vectors. We then assume a single-valued horizon surface $t = f(x, y)$. The surface can be implicitly defined as a set of points (x, y, t) satisfying

$$F(x, y, t) = t - f(x, y) = 0. \tag{1}$$

The defined function $F(x, y, t)$ is 0 everywhere, but its gradient vectors are not zero vectors and can be represented as $\nabla F(x, y, t) = [-\frac{\partial f}{\partial x} - \frac{\partial f}{\partial y} 1]^\top$, where $\|\nabla F(x, y, t)\| \geq 1$. The unit vectors perpendicular to the surface are

$$\mathbf{n}_s = \frac{\nabla F(x, y, t)}{\|\nabla F(x, y, t)\|} = \alpha \begin{bmatrix} -\frac{\partial f}{\partial x} \\ -\frac{\partial f}{\partial y} \\ 1 \end{bmatrix}, \tag{2}$$

where $\alpha = \frac{1}{\|\nabla F(x,y,t)\|}$ are spatially variant scale factors that make $\mathbf{n}_s$ unit vectors. Here, we assume the surface normal vectors always point downward.

We assume that a surface that follows a seismic reflector is a horizon surface of constant geologic time, and seismic normal vectors computed from a seismic amplitude image are unit vectors that are perpendicular to seismic reflectors. Therefore, the seismic horizon we seek is a surface whose normal vectors $\mathbf{n}_s$ must be equal to the seismic normal vectors $\mathbf{n}$ at all positions (x, y, t) on the horizon. However, we initially do not know the positions of the horizon. To solve this problem, we must iteratively update an initial horizontal surface $f^0(x, y)$, by solving the partial differential equations,

$$\alpha^i \begin{bmatrix} -\frac{\partial f^i}{\partial x} \\ -\frac{\partial f^i}{\partial y} \\ 1 \end{bmatrix} \approx \begin{bmatrix} n_x^{i-1} \\ n_y^{i-1} \\ n_t^{i-1} \end{bmatrix}. \tag{3}$$

Here, $f^i(x, y)$ is a surface computed at the ith iteration; $n_x^{i-1} = n_x(x, y, f^{i-1}(x, y))$, $n_y^{i-1} = n_y(x, y, f^{i-1}(x, y))$, and $n_t^{i-1} = n_t(x, y, f^{i-1}(x, y))$ are the components of seismic normal vectors at positions on the surface obtained in the $(i-1)$th iteration. To start this iterative process, we initialize a horizontal surface $f^0(x, y)$ (black lines in Figure 2a) passing through a control point (green circle in Figure 2a) that is located on the seismic horizon we want to extract. This initial surface is then iteratively updated to align with the seismic horizon. In each iteration, we have $\alpha^i = n_t^{i-1}$ from the third equation of equation 3, and then substitute $\alpha^i = n_t^{i-1}$ into the first two equations to obtain the following inverse-gradient problem (Bienati and Spagnolini, 2001; Farnebäck et al., 2007) to update the surface $f^i(x, y)$:

$$\begin{bmatrix} \frac{\partial f^i}{\partial x} \\ \frac{\partial f^i}{\partial y} \end{bmatrix} \approx \begin{bmatrix} p^{i-1} \\ q^{i-1} \end{bmatrix}, \tag{4}$$

where $p^{i-1} = -n_x^{i-1}/n_t^{i-1}$ and $q^{i-1} = -n_y^{i-1}/n_t^{i-1}$ are reflector slopes in the x- and y-directions, respectively. Here, we assume seismic reflectors cannot be vertical and seismic normal vectors always point downward, then $n_t > 0$. These two equations above should be satisfied for every sample on the horizon, but it usually helps to weight these equations by some measure $w(x, y, t)$ of the quality of the estimated reflector slopes. For example, because noise is considered nonplanar in general, $w(x, y, t)$ can be a measure of local

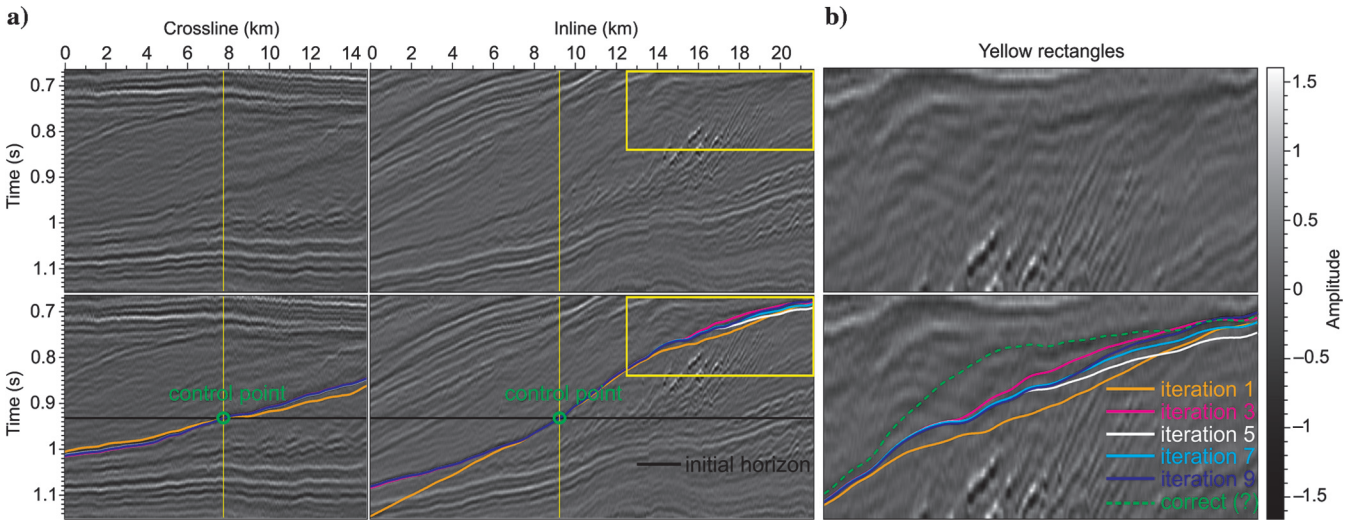

Figure 2. (a) Seismic sections and (b) subsections that intersect with a sequence boundary. The initially horizontal surface (black curve) passes through one control point and is updated iteratively using seismic normal vectors. The dashed green curve denotes the manually interpreted sequence boundary.

planarity in the seismic image, easily computed from structure tensors (Hale, 2009). Then,

$$w^{i-1}\begin{bmatrix}\frac{\partial f^i}{\partial x}\\ \frac{\partial f^i}{\partial y}\end{bmatrix} \approx w^{i-1}\begin{bmatrix}p^{i-1}\\ q^{i-1}\end{bmatrix}, \tag{5}$$

where $w^{i-1} = w(x, y, f^{i-1}(x, y))$. Assuming we have N sampled locations on the horizon surface, we will have $2N$ weighted equations for the N unknowns $f^i(x, y)$. For each iteration, we discretize these equations to obtain the corresponding matrix form:

$$\mathbf{WGf} \approx \mathbf{Wv}, \tag{6}$$

where $\mathbf{W}$ is a $2N \times 2N$ diagonal matrix containing weights $w(x, y, f^{i-1}(x, y))$, $\mathbf{G}$ is a $2N \times N$ sparse matrix obtained by discretizing partial derivatives, $\mathbf{v}$ is a $2N \times 1$ vector containing the seismic reflector slopes p^{i-1} and q^{i-1} on the surface $f^{i-1}(x, y)$ obtained in the previous iteration, and $\mathbf{f}$ is an $N \times 1$ vector containing surface depths $f^i(x, y)$ we want to find. We use approximate equalities in equations 3–6 because we compute the least-squares solution by solving the normal equation of equation 6:

$$(\mathbf{WG})^\top\mathbf{WGf} = (\mathbf{WG})^\top\mathbf{Wv}. \tag{7}$$

To simplify this equation, we let $\mathbf{A} = (\mathbf{WG})^\top\mathbf{WG}$ and $\mathbf{b} = (\mathbf{WG})^\top\mathbf{Wv}$ to obtain

$$\mathbf{Af} = \mathbf{b}. \tag{8}$$

Because the matrix $\mathbf{A} = \mathbf{G}^\top\mathbf{W}^\top\mathbf{WG}$ is symmetric positive definite (SPD), we use the CG method to solve this linear system.

Preconditioner

To accelerate the convergence of CG iterations, we use the model reparameterization technique $\mathbf{f} = \mathbf{S}\tilde{\mathbf{f}}$ (VanDecar and Snieder, 1994; Harlan, 1995; Fomel and Claerbout, 2003). $\mathbf{S}$ is a simplification operator designed to create the desired features in the solution $\mathbf{f}$. Applying this technique to the system of equation 8, we first solve a new system,

$$\mathbf{S}^\top\mathbf{AS}\tilde{\mathbf{f}} = \mathbf{S}^\top\mathbf{b}, \tag{9}$$

for the new unknowns $\tilde{\mathbf{f}}$ and then compute the desired solution $\mathbf{f} = \mathbf{S}\tilde{\mathbf{f}}$. For an appropriate operator $\mathbf{S}$, the CG method applied to the new system of equation 9 converges much faster than for the original system of equation 8. In effect, this model reparameterization is equivalent to split preconditioning (Saad, 1996) with left and right preconditioners $\mathbf{M}_L^{-1} = \mathbf{S}^\top$ and $\mathbf{M}_R^{-1} = \mathbf{S}$. As noted by Saad (1996), this split preconditioning can be implemented with a left preconditioning matrix $\mathbf{M} = \mathbf{M}_L\mathbf{M}_R$ in a preconditioned CG solution of

$$\mathbf{M}^{-1}\mathbf{Af} = \mathbf{M}^{-1}\mathbf{b}, \tag{10}$$

where $\mathbf{M}^{-1} = \mathbf{SS}^\top$. Recall that $\mathbf{S}$ is a simplification operator used to facilitate desired features in the solution (Harlan, 1995). Here, we implement $\mathbf{S}$ as a smoothing operator $\mathbf{S} = \mathbf{S}_x\mathbf{S}_y$, where $\mathbf{S}_x$ and $\mathbf{S}_y$ are axis-aligned smoothing filters in the x and y directions, respectively. A horizon surface $\mathbf{f}$ is often smooth, except at faults. Therefore, our $\mathbf{S}_x$ and $\mathbf{S}_y$ are spatially variant smoothing filters (Hale, 2009), with the extent of smoothing controlled by a measure of discontinuity of seismic reflectors. This measure could be planarity (Hale, 2009) or fault likelihood (Hale, 2013). Here, we use planarity, computed from structure tensors, to control the extent of smoothing in $\mathbf{S}_x$ and $\mathbf{S}_y$.

Now, for each iteration (equation 5) that updates the surface $f^i(x, y)$, we solve equation 8 using the preconditioned CG method with preconditioner

$$\mathbf{M}^{-1} = \mathbf{S}_x\mathbf{S}_y\mathbf{S}_y^\top\mathbf{S}_x^\top. \tag{11}$$

In this way, we iteratively update the surface $t = f(x, y)$ until its normal vectors $\mathbf{n}_s$ are aligned with the seismic normal vectors $\mathbf{n}(x, y, t = f(x, y))$. The updating iteration is terminated when the absolute average update of each sample on the surface is smaller than some small number $\frac{\sum_{j=0}^{N-1}|f^i(x_j,y_j)-f^{i-1}(x_j,y_j)|}{N} < \epsilon_t$, where N is the number of samples on the surface and ϵ_t is an arbitrary small number. In summary, given an initially horizontal surface (black curves in Figure 2) that is inconsistent with any seismic reflector, our method iteratively reduces the difference between the normal vectors $\mathbf{n}_s$ of the surface and the seismic normal vectors $\mathbf{n}(x, y, f(x, y))$ on the surface to obtain a single seismic horizon surface (blue curves in Figure 2).

Results without constraints

In Figure 2, using only one control point to indicate which horizon we want to extract, our method updates the initially horizontal surface to the more nearly correct seismic horizon (blue curves in Figure 2) after nine iterations. The extracted surface is well aligned with the seismic horizon at conformable areas in the left section of Figure 2a. However, in the sections shown in Figure 2b, this iterative method fails to update the horizon surface to the location of the angular unconformity (green dashed curve in Figure 2b). Extracting such a sequence boundary or unconformity is an important but difficult problem in seismic interpretation. From structure tensors, we fail to correctly estimate the discontinuous normal vectors at the unconformity and therefore obtain the incorrect horizon surface shown in Figure 2b. In the next section, we describe a method to more accurately extract a sequence boundary using more control points.

Horizon extraction with constraints

Near unconformities, faults, or in areas where an image is noisy, estimated seismic normal vectors are not accurate enough to automatically obtain a correct sequence boundary or horizon. Therefore, instead of using a fully automatic method, we might manually interpret the seismic image to obtain a more geologically reasonable surface. However, we need not manually interpret the entire horizon. Using a small number of control points as constraints, we solve a constrained least-squares problem to efficiently and more accurately extract a sequence boundary or horizon from a noisy or complex seismic image.

Constrained optimization

As discussed above, in each iteration that updates a horizon surface, we solve a linear system $\mathbf{Af} = \mathbf{b}$ for the vector $\mathbf{f}$ that represents

the surface. Because the matrix $\mathbf{A}$ is SPD, solving this linear system is equivalent to minimizing the following quadratic function of the vector $\mathbf{f}$:

$$F(\mathbf{f}) = \frac{1}{2}\mathbf{f}^\top\mathbf{A}\mathbf{f} - \mathbf{b}^\top\mathbf{f}. \tag{12}$$

Suppose we have a set of n control points $(x_i, y_i, t_i), i = 1, 2, \ldots, n$, and we want to extract a horizon surface that exactly passes through these points. With these constraints, we obtain a constrained optimization problem:

$$\text{minimize}_{\mathbf{f}}\ F(\mathbf{f}) = \frac{1}{2}\mathbf{f}^\top\mathbf{A}\mathbf{f} - \mathbf{b}^\top\mathbf{f}, \quad \text{subject to } \mathbf{C}\mathbf{f} = \mathbf{t}, \tag{13}$$

where $\mathbf{t} = [t_1, t_2, \ldots, t_n]^\top$ is an $n \times 1$ column vector, and $\mathbf{C}$ is an $n \times N$ (where, again, N is the number of samples on the surface) sparse matrix with ones at the positions corresponding to control points and zeros elsewhere. Assuming we have found some solution $\mathbf{f}_0$ to the constraint equation $\mathbf{C}\mathbf{f}_0 = \mathbf{t}$, and a matrix $\mathbf{Z}$ whose columns form a basis for the null space of $\mathbf{C}$ so that $\mathbf{C}\mathbf{Z} = \mathbf{0}$, then any solution $\mathbf{f}$ of the constraint equation $\mathbf{C}\mathbf{f} = \mathbf{t}$ can be written as

$$\mathbf{f} = \mathbf{f}_0 + \mathbf{Z}\mathbf{p}, \tag{14}$$

where $\mathbf{p}$ is a reduced $(N - n) \times 1$ column vector, and again n is the number of control points. The control points must be unique to ensure that the matrix $\mathbf{C}$ has n linearly independent rows and $\mathbf{Z}$ has $N - n$ linearly independent columns.

Substituting equation 14 into equation 12, we obtain a quadratic function $F(\mathbf{p})$ with the reduced vector $\mathbf{p}$:

$$F(\mathbf{p}) = \frac{1}{2}(\mathbf{f_0} + \mathbf{Z}\mathbf{p})^\top\mathbf{A}(\mathbf{f_0} + \mathbf{Z}\mathbf{p}) - \mathbf{b}^\top(\mathbf{f_0} + \mathbf{Z}\mathbf{p}). \tag{15}$$

Minimizing this quadratic function for the reduced solution $\mathbf{p}$ is equivalent to solving the following reduced linear system:

$$\mathbf{Z}^\top\mathbf{A}\mathbf{Z}\mathbf{p} = \mathbf{Z}^\top(\mathbf{b} - \mathbf{A}\mathbf{f}_0). \tag{16}$$

We can now solve this reduced system to get $\mathbf{p}$ and then recover the desired solution $\mathbf{f}$ by using equation 14.

Constrained preconditioner

Before we can solve equation 16, we must find matrix $\mathbf{Z}$ and vector $\mathbf{f}_0$. Fortunately, these subproblems are simple. For example, assume we have three control points: $f_0 = t_0$, $f_2 = t_2$, and $f_3 = t_3$, then $\mathbf{t} = [\,t_0 \quad t_2 \quad t_3\,]^\top$ and the matrix $\mathbf{C}$ is

$$\mathbf{C} = \begin{bmatrix} 1 & 0 & 0 & 0 & 0 & \cdots & 0 \\ 0 & 0 & 1 & 0 & 0 & \cdots & 0 \\ 0 & 0 & 0 & 1 & 0 & \cdots & 0 \end{bmatrix}_{3\times N}. \tag{17}$$

We can immediately find a solution $\mathbf{f}_0 = [\,t_0 \quad 0 \quad t_2 \quad t_3 \quad 0 \cdots 0]^\top$ to the constraint equation $\mathbf{C}\mathbf{f}_0 = \mathbf{t}$. The columns of matrix $\mathbf{Z}$ form a basis of the null space of matrix $\mathbf{C}$, so that $\mathbf{C}\mathbf{Z} = \mathbf{0}$. We generate such a matrix $\mathbf{Z}$ from an $N \times N$ identity matrix, by removing any columns that are identical to rows in the matrix $\mathbf{C}$:

$$\mathbf{Z} = \begin{bmatrix} 0 & 0 & \cdots & 0 \\ 1 & 0 & \cdots & 0 \\ 0 & 0 & \cdots & 0 \\ 0 & 0 & \cdots & 0 \\ 0 & 1 & \cdots & 0 \\ \vdots & \vdots & \ddots & \vdots \\ 0 & 0 & \cdots & 1 \end{bmatrix}_{N\times(N-3)}. \tag{18}$$

Given $\mathbf{Z}$ and the solution $\mathbf{f}_0$, we are ready to solve the reduced system shown in equation 16. Because the matrix $\mathbf{Z}^\top\mathbf{A}\mathbf{Z}$ is SPD, we can use the CG method to solve this reduced system. Many authors (e.g., Nash and Sofer, 1996; Gould et al., 2001; Dollar, 2005) discuss the solution of this system using the preconditioned CG method, and we use a simple preconditioner $\mathbf{P}_z$ described in Nash and Sofer (1996):

$$\mathbf{P}_z = \mathbf{Z}^\top\mathbf{M}^{-1}\mathbf{Z} \approx (\mathbf{Z}^\top\mathbf{A}\mathbf{Z})^{-1}, \tag{19}$$

where $\mathbf{M^{-1}} = \mathbf{S}_x\mathbf{S}_y\mathbf{S}_y^\top\mathbf{S}_x^\top$ as in equation 11, and $\mathbf{Z}^\top\mathbf{Z} = \mathbf{I}$ because the columns of $\mathbf{Z}$ form a basis. Therefore, our preconditioner for the reduced system is

$$\mathbf{P}_z = \mathbf{Z}^\top\mathbf{S}_x\mathbf{S}_y\mathbf{S}_y^\top\mathbf{S}_x^\top\mathbf{Z}. \tag{20}$$

In the preconditioned CG method for the reduced system, one would compute the initial residual $\mathbf{r}_z = \mathbf{Z}^\top(\mathbf{b} - \mathbf{A}\mathbf{f}_0) - \mathbf{Z}^\top\mathbf{A}\mathbf{Z}\mathbf{p}$ and the preconditioned residual $\mathbf{g}_z = \mathbf{P}_z\mathbf{r}_z$.

Instead of solving the reduced system to obtain $\mathbf{p}$ and then recovering the desired solution $\mathbf{f}$, we can instead directly solve for $\mathbf{f}$ because we have a relationship between the reduced and full solutions $\mathbf{f} = \mathbf{f}_0 + \mathbf{Z}\mathbf{p}$. As discussed by Gould et al. (2001), to explicitly perform the multiplication by $\mathbf{Z}$ and the addition of the term $\mathbf{f}_0$ in the CG method, we may choose $\mathbf{f} = \mathbf{f}_0 + \mathbf{Z}\mathbf{p}$, $\mathbf{Z}^\top\mathbf{r} = \mathbf{r}_z$, and $\mathbf{g} = \mathbf{Z}\mathbf{g}_z$, so that $\mathbf{g} = \mathbf{Z}\mathbf{P}_z\mathbf{Z}^\top\mathbf{r}$. This process is equivalent to applying the preconditioned CG method to the unconstrained linear system $\mathbf{A}\mathbf{f} = \mathbf{b}$, with a preconditioner

$$\mathbf{P} = \mathbf{Z}\mathbf{P}_z\mathbf{Z}^\top = \mathbf{Z}\mathbf{Z}^\top\mathbf{M}^{-1}\mathbf{Z}\mathbf{Z}^\top = \mathbf{Z}\mathbf{Z}^\top\mathbf{S}_x\mathbf{S}_y\mathbf{S}_y^\top\mathbf{S}_x^\top\mathbf{Z}\mathbf{Z}^\top. \tag{21}$$

In practice, we do not explicitly form the matrices $\mathbf{A}$ and $\mathbf{Z}\mathbf{Z}^\top$ because the preconditioned CG method requires only the computation of the residual vector $\mathbf{r} = \mathbf{b} - \mathbf{A}\mathbf{f}$ and gradient vector $\mathbf{g} = \mathbf{P}\mathbf{r}$.

It is trivial to compute vector $\mathbf{Z}\mathbf{Z}^\top\mathbf{x}$ for any $N \times 1$ vector $\mathbf{x}$ because $\mathbf{Z}\mathbf{Z}^\top$ has the form

$$\mathbf{Z}\mathbf{Z}^\top = \begin{bmatrix} 0 & 0 & 0 & 0 & 0 & \cdots & 0 \\ 0 & 1 & 0 & 0 & 0 & \cdots & 0 \\ 0 & 0 & 0 & 0 & 0 & \cdots & 0 \\ 0 & 0 & 0 & 0 & 0 & \cdots & 0 \\ 0 & 0 & 0 & 0 & 1 & \cdots & 0 \\ \vdots & \vdots & \vdots & \vdots & \vdots & \ddots & \vdots \\ 0 & 0 & 0 & 0 & 0 & \cdots & 1 \end{bmatrix}_{N\times N}. \tag{22}$$

Computation of $\mathbf{Z}\mathbf{Z}^\top\mathbf{x}$ zeros all the elements of $\mathbf{x}$ with indices corresponding to the locations of control points. With the preconditioner $\mathbf{P}$ denoted by equation 21, the preconditioned gradient $\mathbf{g} = \mathbf{Z}\mathbf{g}_z = \mathbf{Z}\mathbf{P}_z\mathbf{Z}^\top\mathbf{r}$ is projected to be in the null space of $\mathbf{C}$. As

a result, all updates to the solution $\mathbf{f}$ in this preconditioned CG method will also lie in the null space of $\mathbf{C}$. Therefore, because the initial solution $\mathbf{f}_0$ satisfies the constraints $\mathbf{Cf}_0 = \mathbf{t}$, the solution $\mathbf{f}$ after each CG iteration also satisfies $\mathbf{Cf} = \mathbf{t}$.

Results with constraints

Where seismic normal vectors estimated from structure tensors are inaccurate (e.g., near unconformities, faults, and noisy data), the use of control points helps to extract a more reliable horizon or sequence boundary. As shown in Figure 2, when we extract a sequence boundary constrained by only one control point (green circle in Figure 2a), the surface we extract (blue curves in Figure 2b) is well aligned with a seismic reflector in the conformable areas (the left-side section and the left part of the right-side section in Figure 2a), in which seismic normal vectors can be estimated accurately. However, the surface (blue curves) extracted at the unconformity (Figure 2b) deviates from the manually interpreted surface (dashed green curve in Figure 2b) because the normal vectors estimated there are inaccurate. Using 19 control points (green points in Figure 3c), we obtain a surface that better fits the manually interpreted sequence boundary. Figure 3a shows crossline and inline seismic sections that intersect the sequence boundaries extracted using (1) only one control point (blue curves) and (2) 19 control points (green curves). We observe that the sequence boundary extracted using 19 control points better represents the manually interpreted unconformity surface compared with the one extracted using only one control point. Figure 3b and 3c shows the same extracted sequence-boundary surfaces colored with seismic amplitudes. Amplitude values for 19 control points (Figure 3c) are more uniform

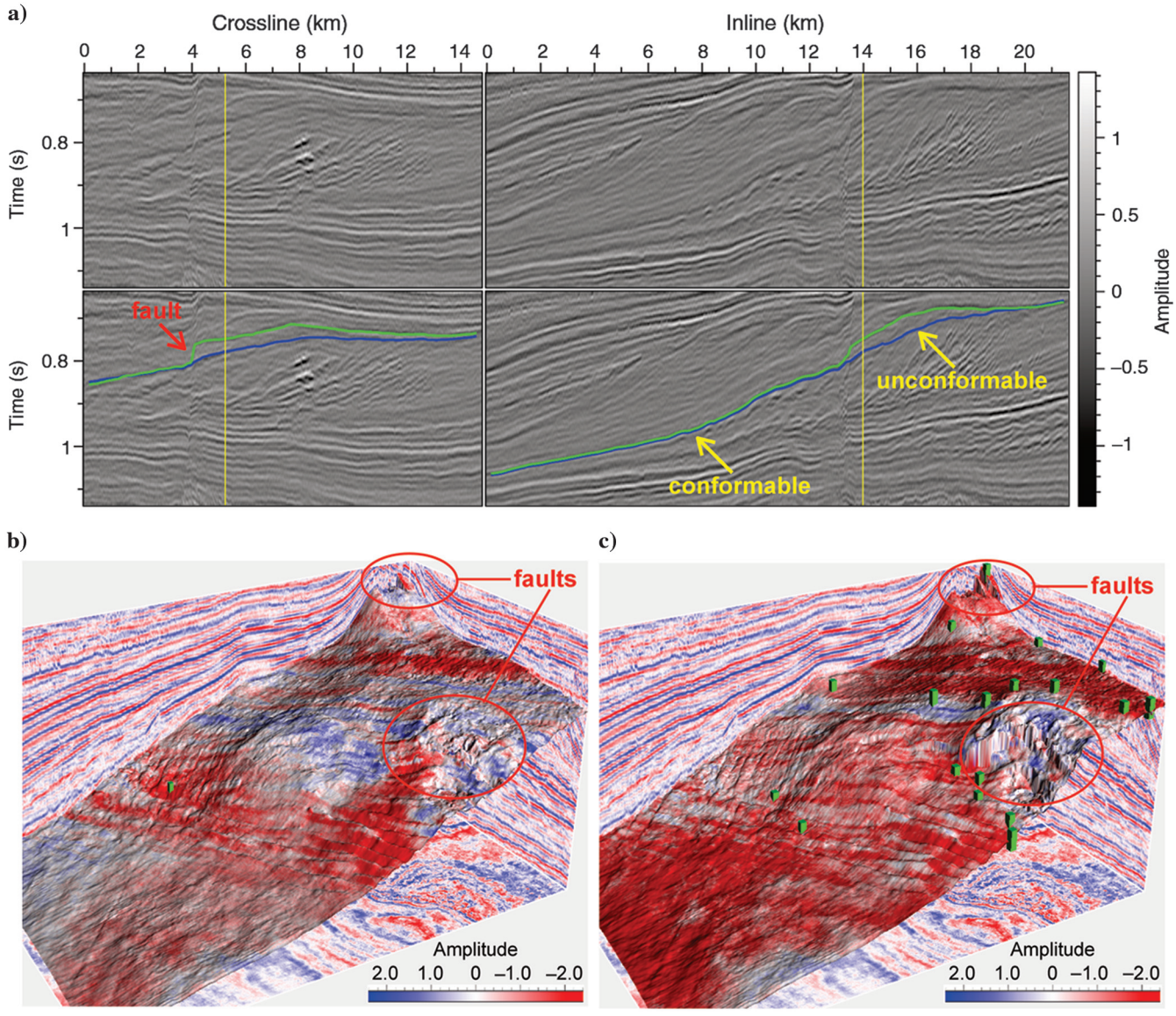

Figure 3. (a) Seismic sections intersect sequence boundaries extracted using one control point (blue curve) and 19 control points (green curve). Panels (b) and (c) show a 3D view of the extracted surfaces using one control point and 19 control points, respectively. Both of the two surfaces are colored by amplitude.

than those for one control point (Figure 3b). This sequence boundary is also complicated by faults, highlighted by red ellipses in Figure 3. The surface extracted using only one control point (blue curves in Figure 3a and the surface in Figure 3b) is inaccurate near faults. However, the surface with 19 control points (green curves in Figure 3a and the surface in Figure 3c) more accurately follows the faults. This example demonstrates that constraints facilitate extraction of a horizon surface complicated by faults. Moreover, with more control points, an initial surface converges more quickly to the final extracted horizon. We can use more control points to interpolate a better initial surface $f^0(x, y)$ that is smooth but exactly passes through the control points. An initial surface interpolated using more control points will be closer to the seismic horizon $f(x, y)$ we want to extract, which therefore enables the CG method to more quickly converge to that horizon. For example, it takes nine iterations to converge using one control point (blue curves in Figure 3a), but only five iterations to converge using 19 control points (green curves in Figure 3a).

GENERATING A HORIZON VOLUME

Using the method discussed above, we can extract a single seismic horizon or sequence boundary with one or more control points that represent interpreted constraints. With similar constraints, we can also extract all seismic horizons from a seismic image at once, and thereby we can generate a complete horizon volume. In a horizon volume $t(x, y, \tau)$, as shown in Figure 1c, the vertical axis is RGT τ and color denotes seismic traveltime t. Horizontally slicing a horizon volume at any single RGT value τ yields a seismic horizon. Here, we first describe a method for using seismic normal vectors to automatically generate a horizon volume without constraints, which is usually accurate for seismic images with simple structures. To better handle images complicated by faults or noise, we then extend this method, by incorporating scattered sets of interpreted points that correspond to multiple seismic horizons, to generate a more reliable horizon volume that honors those interpreted constraints.

Horizon volume without constraints

As discussed by Parks (2010), a horizon volume $t(x, y, \tau)$ can be generated from an RGT volume $\tau(x, y, t)$ by inverse linear interpolation if we assume that τ in the RGT volume increases monotonically with seismic traveltime t. Some authors have described methods to generate such an RGT volume using phase unwrapping (e.g., Stark, 2003, 2004; Wu and Zhong, 2012a) or reflector dips (Fomel, 2010; Parks, 2010). Here, we rederive the method of Parks (2010) in a simpler way to compute an RGT volume. In an RGT volume $\tau(x, y, t)$ like that shown in Figures 4a or 1b, contours (Figure 4b) of constant τ represent seismic horizons, which means that these contours should have the same structures as seismic reflectors in the seismic image (Figure 4b). Therefore, gradient vectors for an RGT volume $\tau(x, y, t)$, which are perpendicular to RGT contours, should be parallel to seismic normal vectors $\mathbf{n} = [n_x, n_y, n_t]^\top$, which are perpendicular to seismic amplitude reflectors. If we assume that these vectors always point downward, we have

$$\begin{bmatrix} \frac{\partial \tau}{\partial x} \\ \frac{\partial \tau}{\partial y} \\ \frac{\partial \tau}{\partial t} \end{bmatrix} \approx \alpha \begin{bmatrix} n_x \\ n_y \\ n_t \end{bmatrix}, \tag{23}$$

where α is a positive and spatially variant scalar number. Because we again have more equations than unknowns, in general, we can only approximately solve these coupled partial differential equations. Because we assume that all the seismic normal vectors are always point downward, which means that the vertical component n_t of the normal vectors are always positive ($n_t > 0$). Therefore, RGT results computed using the partial differential equations above usually increase vertically with traveltime. Using the third equation of equation 23, we compute $\alpha = (\partial\tau/\partial t)/n_t$, where $n_t > 0$. Substituting α into the first two of equation 23, we obtain

$$\begin{bmatrix} n_t \frac{\partial \tau}{\partial x} - n_x \frac{\partial \tau}{\partial t} \\ n_t \frac{\partial \tau}{\partial y} - n_y \frac{\partial \tau}{\partial t} \end{bmatrix} \approx \begin{bmatrix} 0 \\ 0 \end{bmatrix}. \tag{24}$$

In attempting to solve these equations, we would need to carefully choose boundary conditions to avoid obtaining the trivial solution $\tau =$ constant. To avoid this problem, as discussed by Parks (2010), we rewrite $\tau(x, y, t)$ as

$$\tau(x, y, t) = t + s(x, y, t), \tag{25}$$

where the function $s(x, y, t)$ represents vertical shifts. Substituting equation 25 into equation 24, we obtain

$$\begin{bmatrix} n_t \frac{\partial s}{\partial x} - n_x \frac{\partial s}{\partial t} \\ n_t \frac{\partial s}{\partial y} - n_y \frac{\partial s}{\partial t} \end{bmatrix} \approx \begin{bmatrix} n_x \\ n_y \end{bmatrix} \tag{26}$$

or

$$\begin{bmatrix} -\frac{\partial s}{\partial x} - p \frac{\partial s}{\partial t} \\ -\frac{\partial s}{\partial y} - q \frac{\partial s}{\partial t} \end{bmatrix} \approx \begin{bmatrix} p \\ q \end{bmatrix}, \tag{27}$$

where again $p = -n_x/n_t$ and $q = -n_y/n_t$ are estimated slopes of seismic reflectors in x- and y-directions. Equation 27 is what Parks (2010) solved to obtain shifts that flatten a seismic image. As suggested by Lomask et al. (2006), we add a third equation $\epsilon s_t \approx 0$ to reduce vertical variations in the shifts. We also weight the equations above by a measure $w(x, y, t)$ of the quality of the estimated reflector slopes $p(x, y, t)$ and

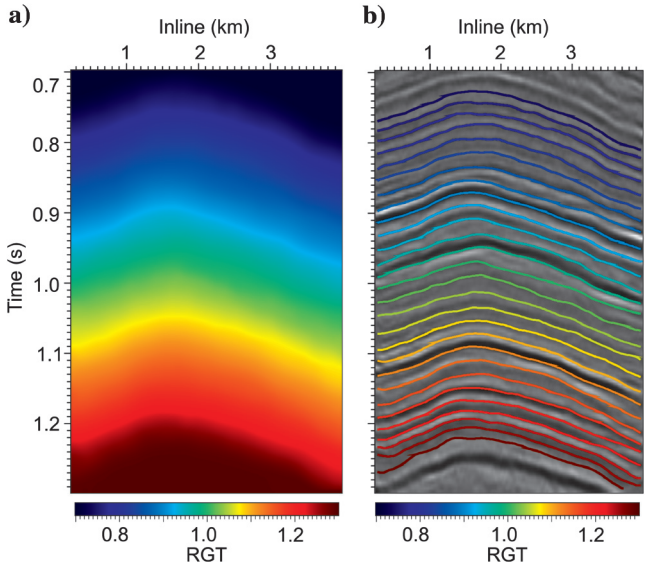

Figure 4. The same (a) RGT volume as shown in Figure 1b, and (b) contours of the RGT volume are horizons in the corresponding seismic image.

$q(x, y, t)$. We then compute the shifts by solving the following equations:

$$\begin{bmatrix} w\left(-\frac{\partial s}{\partial x} - p\frac{\partial s}{\partial t}\right) \\ w\left(-\frac{\partial s}{\partial y} - q\frac{\partial s}{\partial t}\right) \\ \epsilon\frac{\partial s}{\partial t} \end{bmatrix} \approx \begin{bmatrix} wp \\ wq \\ 0 \end{bmatrix}. \tag{28}$$

If we have N image samples, then equation 28 represents $3N$ equations for N unknown shifts, and these equations can be expressed in matrix form as

$$\mathbf{WGs} \approx \mathbf{Wv}, \tag{29}$$

where $\mathbf{s}$ is an $N \times 1$ vector containing the unknown shifts $s(x, y, t)$, $\mathbf{G}$ is a $3N \times N$ sparse matrix representing finite-difference approximations of partial derivatives, $\mathbf{W}$ is a $3N \times 3N$ diagonal matrix containing weights $w(x, y, t)$ and the constant ϵ, and $\mathbf{v}$ is a $3N \times 1$ vector with $2N$ slopes p and q, and N zeros.

From equations 23–29, we use the approximate equalities because we compute the least-squares solution by solving the normal equation of equation 29:

$$(\mathbf{WG})^\top\mathbf{WGs} = (\mathbf{WG})^\top\mathbf{Wv}. \tag{30}$$

Let $\mathbf{A} = (\mathbf{WG})^\top\mathbf{WG}$ and $\mathbf{b} = (\mathbf{WG})^\top\mathbf{Wv}$ so that this linear system becomes

$$\mathbf{As} = \mathbf{b}. \tag{31}$$

The matrix $\mathbf{A}$ is SPD and sparse. In practice, we do not explicitly form the matrices $\mathbf{A}$, $\mathbf{W}$, and $\mathbf{G}$. Instead, we solve this linear system using the CG method, which requires only the computation of matrix-vector products such as $\mathbf{As} = (\mathbf{WG})^\top\mathbf{WGs}$ and $\mathbf{b} = (\mathbf{WG})^\top\mathbf{Wv}$. As when extracting a single seismic horizon, we solve equation 31 using the preconditioned CG method with a preconditioner defined by

$$\mathbf{M^{-1}} = \mathbf{S}_x\mathbf{S}_y\mathbf{S}_t\mathbf{S}_t^\top\mathbf{S}_y^\top\mathbf{S}_x^\top, \tag{32}$$

where, again, $\mathbf{S}_x$, $\mathbf{S}_y$, and $\mathbf{S}_t$ are filters that smooth in the x-, y-, and t-directions, respectively. We again expect the solution to be laterally smooth except at faults. Therefore, the lateral smoothing filters $\mathbf{S}_x$ and $\mathbf{S}_y$ are spatially variant filters (Hale, 2009), and the extent of smoothing is proportional to a measure of reflector continuity, so that these filters smooth less at faults.

We expect the shifts to be vertically smooth because we assume that there are no unconformities in this example. Therefore, our vertical smoothing filter $\mathbf{S}_t$ in this example is spatially invariant. We derive all of the equations above for 3D images, but they can be easily modified to work for 2D images, by omitting the second equation for the y-direction from equation 28. For the 2D example shown in Figure 1, we first solved equation 31 to get shifts $s(x, t)$. We then computed an RGT volume $\tau(x, t) = t + s(x, t)$ (Figure 1b), where τ increases monotonically (τ does not decrease, but increases with different rates) with seismic traveltime t. Finally, we computed a horizon volume $t(x, \tau)$ (Figure 1c) from the RGT volume $\tau(x, t)$ by inverse linear interpolation (Parks, 2010). This horizon volume

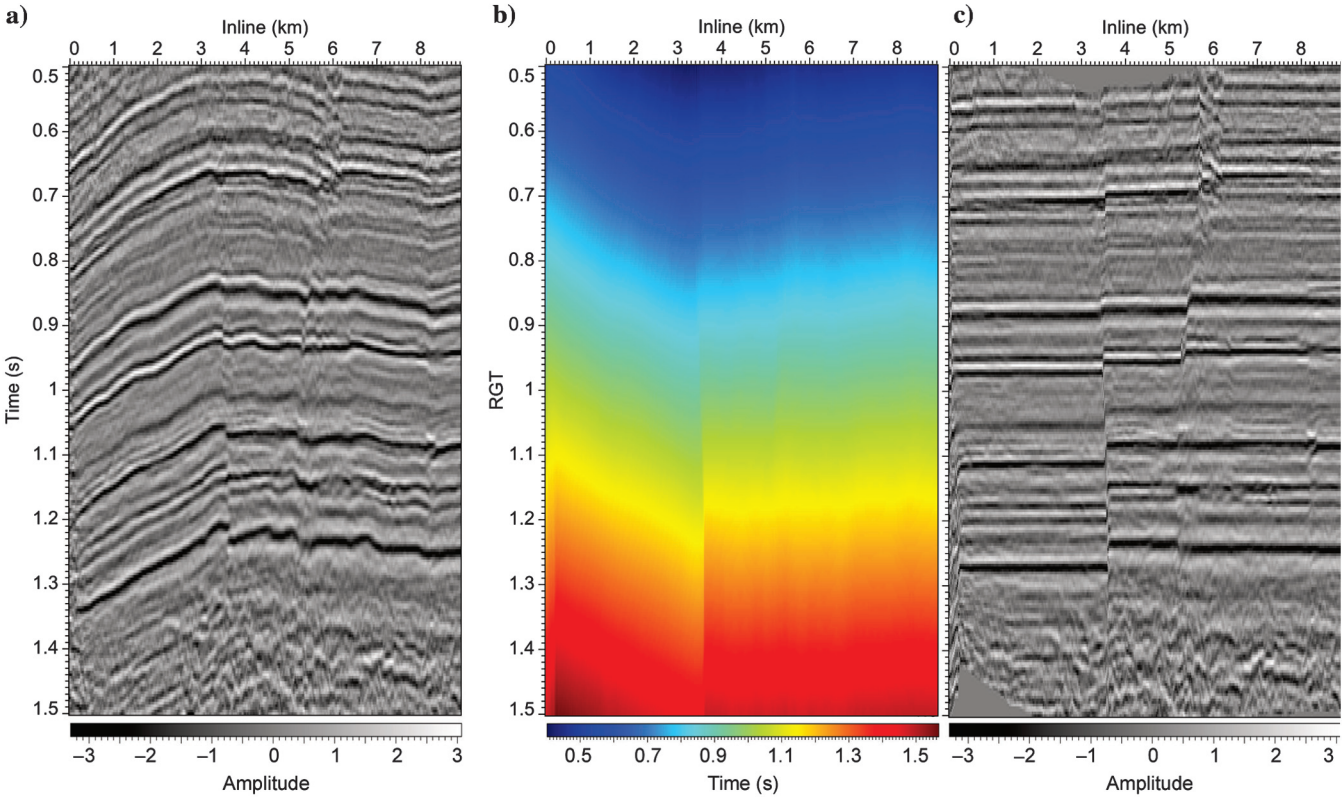

Figure 5. (a) A seismic image, (b) generated horizon volume, and (c) flattened image without control points.

$t(x, \tau)$ maps the seismic image (Figure 1a) to a flattened image (Figure 1d).

For seismic images with simple geologic structures and little noise, as in Figure 1a, we can use the method discussed above to compute an accurate RGT volume (Figure 1b). A horizon volume (Figure 1c) is then interpolated from the RGT volume and subsequently used to flatten the input seismic image (Figure 1a) to produce the flattened image (Figure 1d). However, for seismic images complicated by faults, as in Figure 5a, the generated horizon volume (Figure 5b) is inaccurate, so that the seismic reflectors are not flattened correctly (Figure 5c). Therefore, we extend this method to compute more accurate RGT and horizon volumes by incorporating one set or multiple sets of interpreted control points that may correspond to one or multiple horizons, without defining any RGT values for any control points.

Horizon volume with constraints

For specified sets of control points, we solve a constrained optimization problem similar to that we solve when extracting a single seismic horizon:

$$\text{minimize}_{\mathbf{s}}\, F(\mathbf{s}) = \frac{1}{2}\mathbf{s}^{\top}\mathbf{A}\mathbf{s} - \mathbf{b}^{\top}\mathbf{s}, \quad \text{subject to } \mathbf{C}\mathbf{s} = \mathbf{d}. \tag{33}$$

As when extracting a single horizon, solving the constrained problem above is equivalent to solving a corresponding unconstrained problem $\mathbf{A}\mathbf{s} = \mathbf{b}$ using a preconditioned CG method with an initial solution $\mathbf{s}_0$ to the constraint equation $\mathbf{C}\mathbf{s}_0 = \mathbf{d}$ and a constrained preconditioner $\mathbf{P} = \mathbf{Z}\mathbf{Z}^{\top}\mathbf{M}^{-1}\mathbf{Z}\mathbf{Z}^{\top}$, where $\mathbf{M}^{-1} = \mathbf{S}_x\mathbf{S}_y\mathbf{S}_t\mathbf{S}_t^{\top}\mathbf{S}_y^{\top}\mathbf{S}_x^{\top}$. Therefore, to solve this problem, we need only an initial solution $\mathbf{s}_0$ and the matrix $\mathbf{Z}\mathbf{Z}^{\top}$ for the preconditioner $\mathbf{P}$.

Let us use a tiny 3D seismic image with only $N = 2 \times 2 \times 2$ samples to explain how to implement multiplication by the matrix $\mathbf{Z}\mathbf{Z}^{\top}$ and to find an initial solution $\mathbf{s}_0$. As in equation 25, we want to compute a 3D RGT volume $\tau(x, y, t)$ with shifts $s(x, y, t)$. In this simple example, τ and s have only $N = 2 \times 2 \times 2$ samples, and we can express equation 25 in vector form as

$$\boldsymbol{\tau} = \mathbf{t} + \mathbf{s}, \tag{34}$$

where

$$\begin{aligned}
\mathbf{t} &= [\, t_0 \quad t_1 \quad t_2 \quad t_3 \quad t_4 \quad t_5 \quad t_6 \quad t_7 \,]^{\top}, \\
\mathbf{s} &= [\, s_0 \quad s_1 \quad s_2 \quad s_3 \quad s_4 \quad s_5 \quad s_6 \quad s_7 \,]^{\top}, \\
\boldsymbol{\tau} &= [\, \tau_0 \quad \tau_1 \quad \tau_2 \quad \tau_3 \quad \tau_4 \quad \tau_5 \quad \tau_6 \quad \tau_7 \,]^{\top}.
\end{aligned} \tag{35}$$

Assume that we have two sets of constraints: The first set has three control points with sample indices $\{3, 5, 7\}$, and the second set has two control points with sample indices $\{1, 6\}$. Within each set of constraints, all control points are interpreted to be on a single seismic horizon. Therefore, we have $\tau_3 = \tau_5 = \tau_7$ and $\tau_1 = \tau_6$. According to equation 34, this means that $s_5 - s_3 = t_3 - t_5$, $s_7 - s_3 = t_3 - t_7$, and $s_6 - s_1 = t_1 - t_6$. We can therefore write the constraint equation $\mathbf{C}\mathbf{s} = \mathbf{d}$ as follows:

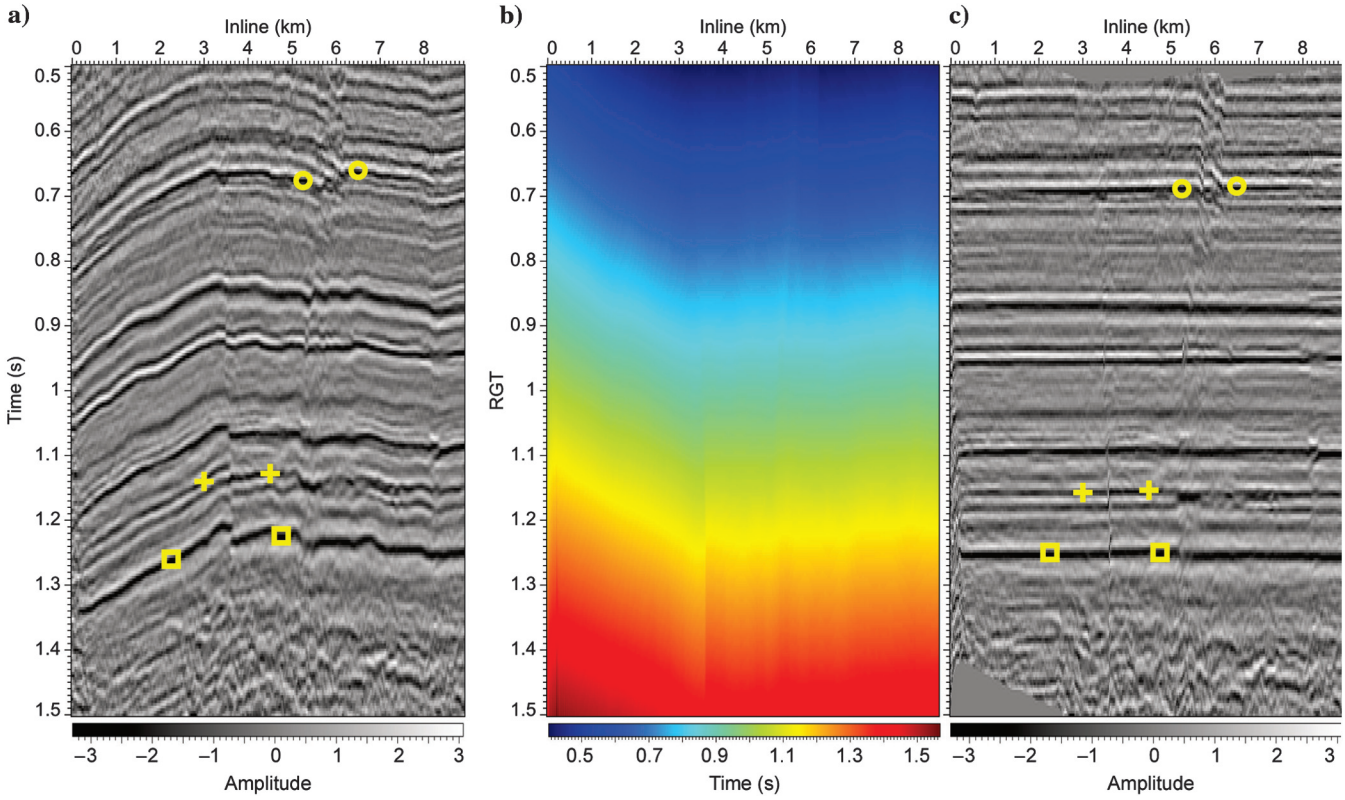

Figure 6. (a) A seismic image with three pairs of interactively interpreted control points (yellow circles, pluses, and squares), (b) generated horizon volume, and (c) flattened image.

$$\begin{bmatrix} 0 & 0 & 0 & -1 & 0 & 1 & 0 & 0 \\ 0 & 0 & 0 & -1 & 0 & 0 & 0 & 1 \\ 0 & -1 & 0 & 0 & 0 & 0 & 1 & 0 \end{bmatrix} \mathbf{s} = \begin{bmatrix} t_3 - t_5 \\ t_3 - t_7 \\ t_1 - t_6 \end{bmatrix}, \quad (36)$$

where, again, $\mathbf{s} = [s_0 \quad s_1 \quad s_2 \quad s_3 \quad s_4 \quad s_5 \quad s_6 \quad s_7]^\top$. Here, we want to emphasize that we do not specify any RGT values or shifts for the interpreted control points to constrain the generation of an RGT or horizon volume. We only set the RGT values of the control points belonging to a same horizon to be equal to construct the constraint equation in 36. This makes it easy for an interpreter to incorporate control points for generating a more reliable horizon volume. In this example, matrix $\mathbf{C}$ has three linearly independent rows so that matrix $\mathbf{Z}$ must have $N-3$ linearly independent columns, such that $\mathbf{CZ} = \mathbf{0}$ because the columns of matrix $\mathbf{Z}$ form a basis for the null space of $\mathbf{C}$. Construction of matrix $\mathbf{Z}$ is only slightly more complicated than for the single-horizon case. Specifically,

$$\mathbf{Z} = [\mathbf{e}_{c1}|\mathbf{e}_{c2}|\mathbf{e}_0|\mathbf{e}_2|\mathbf{e}_4] = \begin{bmatrix} 0 & 0 & 1 & 0 & 0 \\ 0 & 1 & 0 & 0 & 0 \\ 0 & 0 & 0 & 1 & 0 \\ 1 & 0 & 0 & 0 & 0 \\ 0 & 0 & 0 & 0 & 1 \\ 1 & 0 & 0 & 0 & 0 \\ 0 & 1 & 0 & 0 & 0 \\ 1 & 0 & 0 & 0 & 0 \end{bmatrix}_{8\times 5}, \quad (37)$$

where $\mathbf{e}_{c1} = \mathbf{e}_3 + \mathbf{e}_5 + \mathbf{e}_7$, $\mathbf{e}_{c2} = \mathbf{e}_1 + \mathbf{e}_6$, and $\mathbf{e}_i$, for $i = 0, 1, \ldots, N-1$, is an $N \times 1$ unit vector with 1 at the ith index. In other words, we begin with the identity matrix and sum the unit vectors $\mathbf{e}_i$ with indices i in $\{3, 5, 7\}$, corresponding to the first set of control points, to obtain the first column of $\mathbf{Z}$; similarly, we obtain the second column of $\mathbf{Z}$, corresponding to the second set of control points with indices $\{1, 6\}$; and finally, we use all of the remaining unit vectors $\mathbf{e}_i$ that do not correspond to any control point for remaining columns of $\mathbf{Z}$. In the same way, we can easily construct matrix $\mathbf{Z}$ for any number of sets of control points. We can normalize the columns of matrix $\mathbf{Z}$ to obtain

$$\mathbf{Z} = \begin{bmatrix} 0 & 0 & 1 & 0 & 0 \\ 0 & \frac{1}{\sqrt{2}} & 0 & 0 & 0 \\ 0 & 0 & 0 & 1 & 0 \\ \frac{1}{\sqrt{3}} & 0 & 0 & 0 & 0 \\ 0 & 0 & 0 & 0 & 1 \\ \frac{1}{\sqrt{3}} & 0 & 0 & 0 & 0 \\ 0 & \frac{1}{\sqrt{2}} & 0 & 0 & 0 \\ \frac{1}{\sqrt{3}} & 0 & 0 & 0 & 0 \end{bmatrix}_{8\times 5} \quad (38)$$

with columns that form an orthonormal basis for the null space of matrix $\mathbf{C}$. We then find that

$$\mathbf{ZZ}^\top = \begin{bmatrix} 1 & 0 & 0 & 0 & 0 & 0 & 0 & 0 \\ 0 & \frac{1}{2} & 0 & 0 & 0 & 0 & \frac{1}{2} & 0 \\ 0 & 0 & 1 & 0 & 0 & 0 & 0 & 0 \\ 0 & 0 & 0 & \frac{1}{3} & 0 & \frac{1}{3} & 0 & \frac{1}{3} \\ 0 & 0 & 0 & 0 & 1 & 0 & 0 & 0 \\ 0 & 0 & 0 & \frac{1}{3} & 0 & \frac{1}{3} & 0 & \frac{1}{3} \\ 0 & \frac{1}{2} & 0 & 0 & 0 & 0 & \frac{1}{2} & 0 \\ 0 & 0 & 0 & \frac{1}{3} & 0 & \frac{1}{3} & 0 & \frac{1}{3} \end{bmatrix}_{8\times 8}. \quad (39)$$

For any vector $\mathbf{x} = [x_0 \; x_1 \; x_2 \; x_3 \; x_4 \; x_5 \; x_6 \; x_7]^\top$, it is easy to compute the product

$$\mathbf{ZZ}^\top\mathbf{x} = [x_0 \; x_{c2} \; x_2 \; x_{c1} \; x_4 \; x_{c1} \; x_{c2} \; x_{c1}]^\top, \quad (40)$$

where $x_{c1} = (x_3 + x_5 + x_7)/3$ and $x_{c2} = (x_1 + x_6)/2$. In other words, we compute $\mathbf{ZZ}^\top\mathbf{x}$ by

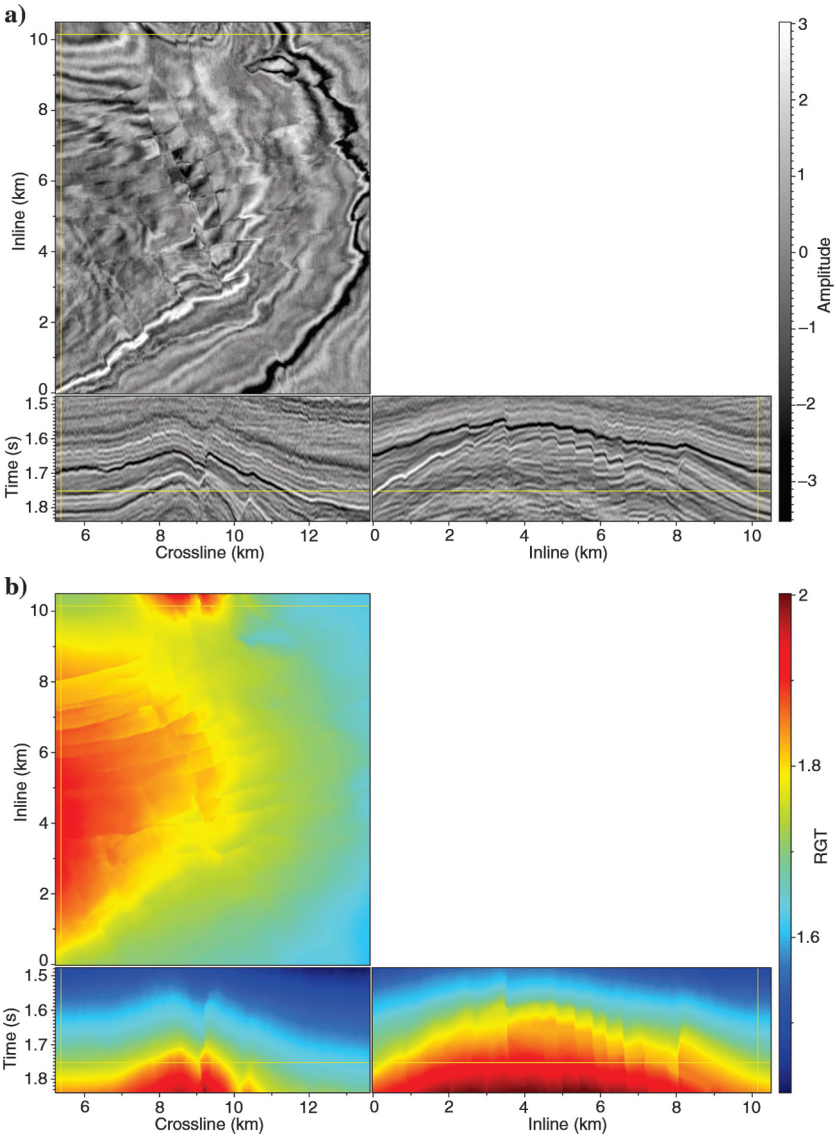

Figure 7. (a) Input seismic image and (b) a corresponding RGT volume computed with three sets of control points.

gathering and averaging all elements of $\mathbf{x}$ with indices corresponding to each set of control points and then scattering the averages back into those same elements. In each CG iteration, when we apply the constrained preconditioner $\mathbf{P} = \mathbf{Z}\mathbf{Z}^\top\mathbf{S}_x\mathbf{S}_y\mathbf{S}_t\mathbf{S}_t^\top\mathbf{S}_y^\top\mathbf{S}_x^\top\mathbf{Z}\mathbf{Z}^\top$ to a vector, we need only to compute averages and apply smoothing filters. We can also easily find an initial solution s_0 to the constraint equation $\mathbf{C}\mathbf{s}_0 = \mathbf{d}$:

$$s_0 = [0 \quad s_1 \quad 0 \quad s_3 \quad 0 \quad s_5 \quad s_6 \quad s_7]^\top, \tag{41}$$

in which elements with indices corresponding to the first set of control points are $s_3 = 0$, $s_5 = t_3 - t_5$, and $s_7 = t_3 - t_7$; elements corresponding to the second set of control points are $s_1 = 0$ and $s_6 = t_1 - t_6$. Therefore, to construct an initial set of shifts $\mathbf{s}_0$, we use zeros for elements that do not correspond to any control points; for each set of control points, we first compute their average depth or traveltime and then choose the point with depth nearest to that average as the reference point and set it with zero shift (e.g., $s_3 = 0$ for the first set of control points, and $s_1 = 0$ for the second set of control points), then use the depth differences between the reference point and other control points for the remaining initial shifts in $\mathbf{s}_0$.

With an initial solution $\mathbf{s}_0$ and the constrained preconditioner $\mathbf{P} = \mathbf{Z}\mathbf{Z}^\top\mathbf{M}^{-1}\mathbf{Z}\mathbf{Z}^\top$, we can apply the preconditioned CG method to the unconstrained system $\mathbf{A}\mathbf{s} = \mathbf{b}$ to obtain a solution $\mathbf{s}$ that satisfies the constrained problem of equation 33. In each CG iteration, we compute a residual as $\mathbf{r} = \mathbf{b} - \mathbf{A}\mathbf{s}$. Using the constrained preconditioner $\mathbf{P}$, we compute a constrained residual $\mathbf{r}_\mathrm{P} = \mathbf{Z}\mathbf{Z}^\top\mathbf{M}^{-1}\mathbf{Z}\mathbf{Z}^\top\mathbf{r}$ that is in the null space of the constraint matrix $\mathbf{C}$. This means that all of the updates to the initial solution $\mathbf{s}_0$ in this preconditioned CG method will also be in the null space of $\mathbf{C}$. Therefore, because the initial solution $\mathbf{s}_0$ satisfies the constraint equation $\mathbf{C}\mathbf{s}_0 = \mathbf{d}$, the final solution $\mathbf{s}$ obtained after any number of CG iterations will also satisfy the constraints. Figure 6 is a 2D example that shows how constraints help to generate a more accurate horizon volume and better flatten a seismic image. In this example, we use the same input seismic image (Figure 6a) complicated by faults that is displayed in Figure 5a, but now we have three sets of constraints. For each set of constraints, we interpret two control points (yellow circles, pluses, and squares in Figure 6a) for each seismic horizon. Using three sets of constraints, we compute a more accurate horizon volume (Figure 6b), with which we can better flatten (Figure 6c) seismic reflectors across faults.

3D results with constraints

Figure 7a shows a 3D seismic image that is also complicated by faults. To flatten this 3D image or generate a horizon volume, we choose weights $w(x, y, t)$ corresponding to faults in equation 28. Specifically, we use the method developed by Hale (2013) to first compute an image of fault likelihoods $f(x, y, t) \in [0, 1]$ in which values near 1 indicate fault locations. We then use $w = (1 - f)^8$ as weights in equation 28, where the power 8 is an arbitrary number to increase the contrast between low and high fault likelihoods. For this example, we use three sets of constraints, corresponding to three horizons in the 3D seismic image, to compute a more accurate horizon volume and more accurately flatten the seismic image. The first set contains five control points, the second one contains seven control points (green points in Figure 8a), and the third one contains 11 control points (green points in Figure 8b). Using these three sets of constraints, we first compute an RGT volume as shown in Figure 7b, from which we then interpolate a horizon volume (Figure 9a) that flattens (Figure 8a or 8b) seismic reflectors across faults. The constraints help to flatten not only reflectors passing through the control points but also other reflectors

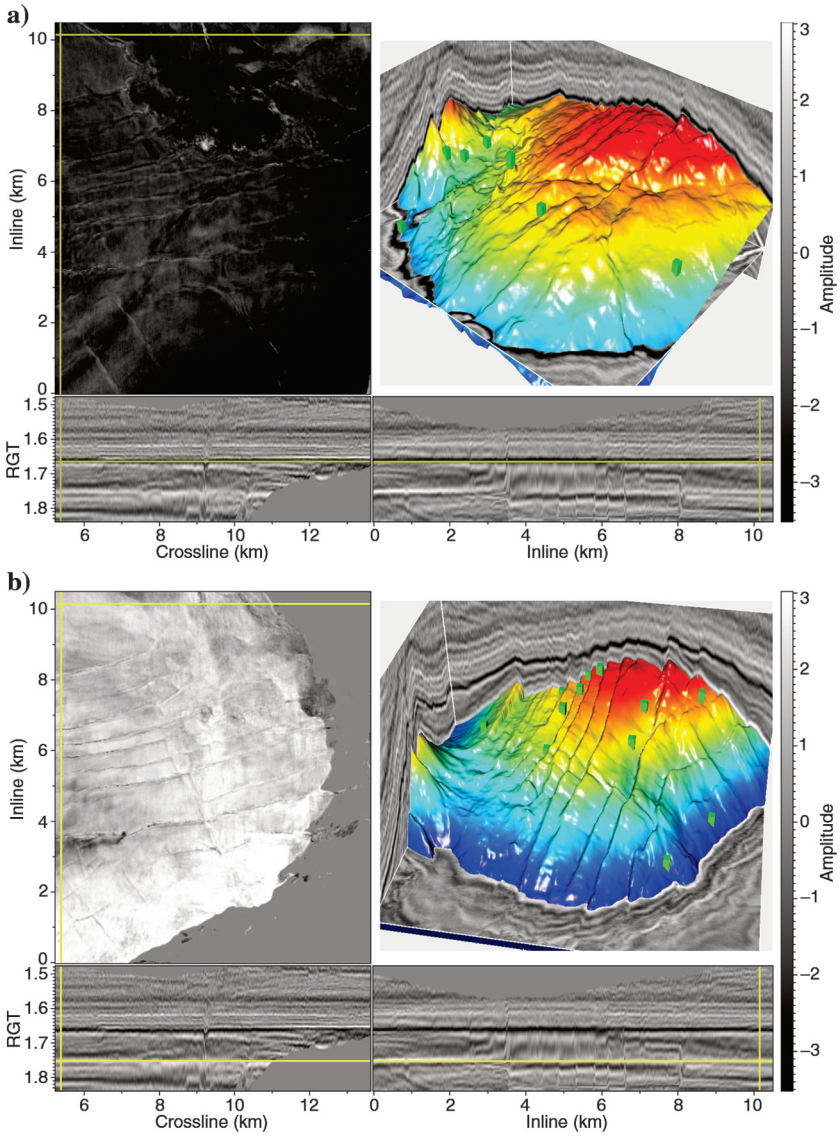

Figure 8. The flattened seismic image is sliced at (a) $\tau = 1.664$ and (b) $\tau = 1.751$. Horizontal slices in a flattened image correspond to seismic horizon surfaces (upper right panels in [a] and [b], for which color denotes depth) in an unflattened image.

in the 3D seismic image as well. Figure 9a displays the horizon volume computed from the RGT volume shown in Figure 7b. Each horizontal slice in the horizon volume is a traveltime structure map of a horizon corresponding to a constant RGT value. Figure 9b shows a 3D view of six seismic horizons extracted by horizontally slicing (h1 ∼ h6 in Figure 9a) the horizon volume at six different RGT values. In Figure 9b, different colors denote different seismic horizons corresponding to the horizontal slices (h1 ∼ h6) with different colors in Figure 9a, but deeper horizons are obscured by the top one. We therefore, in Figure 9c, display cut-away views of each of the horizons. We observe that the horizons with control points (the cyan and yellow surfaces) and others without control points coincide well with seismic reflectors.

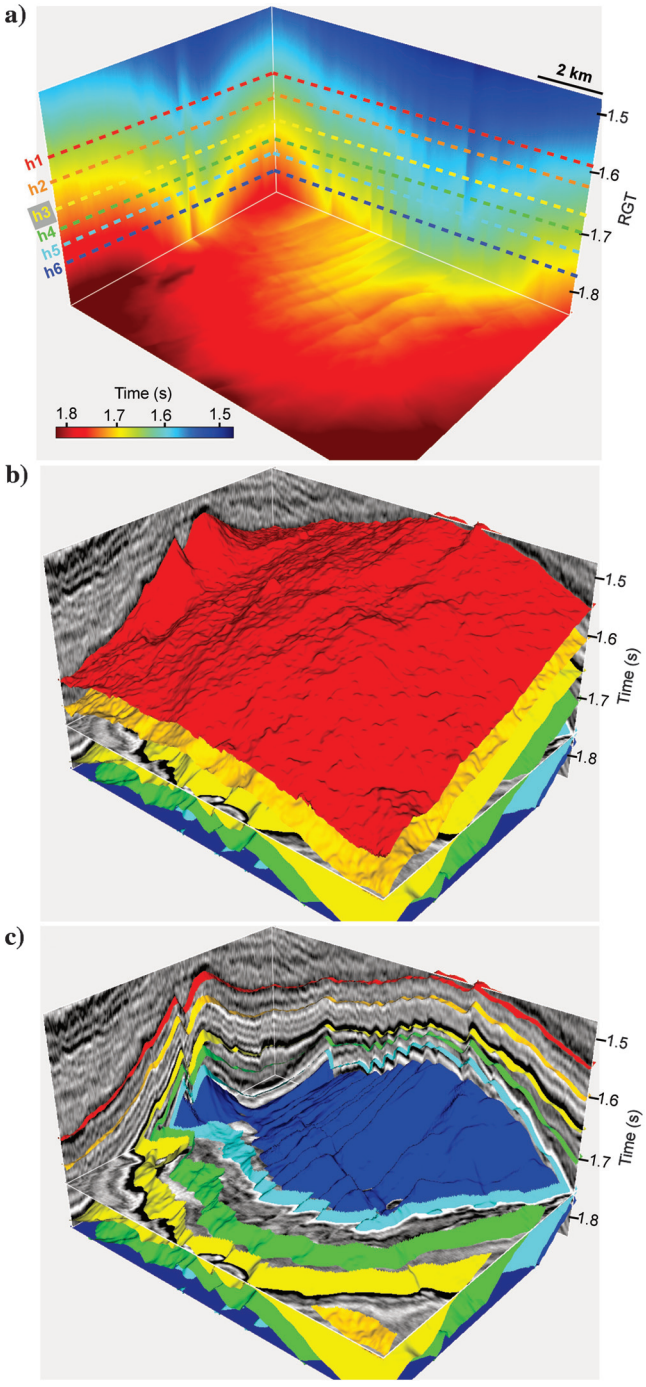

Figure 9. (a) The RGT volume shown in Figure 7b is converted to a complete horizon volume, in which horizontally slicing (h1 ∼ h6) at six different RGT values yields six seismic horizons displayed in panel (b). The cut-away views of these six horizons are shown in panel (c) to reveal more details.

CONCLUSION

We propose methods to (1) extract one seismic horizon at a time and (2) to compute at once a complete horizon volume. We designed these two methods to compute horizons that honor interpreted constraints, specified as sets of control points. We incorporate the control points with simple constraint preconditioners in the CG method used to compute horizons. The first method is useful, even though we can extract all horizons at once using the second method, because it can more quickly extract a single horizon. Using multiple control points, this method can reliably extract complicated geologic surfaces such as sequence boundaries and horizons with faults. Furthermore, this first method might be used to efficiently extract horizons that might serve as control surfaces (large sets of control points) for the second method. The second method generates a complete horizon volume at once. With a small number of interpreted constraints, this method works well for seismic images complicated by faults. Interpreted constraints are necessary because completely automatic interpretation cannot yet handle complicated seismic horizons. The proposed methods provide an especially simple way to specify such constraints by interactively picking points in a 3D seismic image that belong to the same seismic horizon. These methods can be implemented to interactively add or move control points, while quickly updating a single seismic horizon or complete horizon volume. One minor defect of both methods is that they do not automatically produce gaps representing heaves at faults in an extracted horizon, but a postprocessing step can be added to detect possible fault positions from the discontinuities of the extracted horizon surface and then create such gaps at the detected faults. These methods might be further improved if we could predict areas in which control points are required to generate more reliable results so that the interpretation of constraints could be more straightforward and efficient.

ACKNOWLEDGMENTS

This research is supported by the sponsor companies of the Consortium Project on Seismic Inverse Methods for Complex Structures. The real seismic images in the 2D examples shown in Figures 1, 4, 5, and 6 are provided by the U.S. Department of Energy. The real seismic images in the 3D examples shown in Figures 2, 3, 7, 8, and 9 are provided by dGB Earth Sciences.

REFERENCES

Bienati, N., and U. Spagnolini, 2001, Multidimensional wavefront estimation from differential delays: IEEE Transactions on Geoscience and Remote Sensing, **39**, 655–664, doi: 10.1109/36.911122.

Brouwer, F., P. Groot, and M. Kumpus, 2011, Maximizing the value of seismic data through increased horizon mapping: Applications in the Middle East and Canada: First Break, **29**, 87–92.

Burnett, W., and S. Fomel, 2009, Moveout analysis by time-warping: 79th Annual International Meeting, SEG, Expanded Abstracts, 3710–3714.

Clark, J., J. Lomask, and J. Rickett, 2010a, Method for determining geological information related to a subsurface volume of interest: U.S. Patent 7,769,545.
Clark, J., J. Lomask, and J. Rickett, 2010b, Method for indexing a subsurface volume for the purpose of inferring geologic information: U.S. Patent 7,769,546.
De Groot, P., A. Huck, G. de Bruin, N. Hemstra, and J. Bedford, 2010, The horizon cube: A step change in seismic interpretation!: The Leading Edge, **29**, 1048–1055, doi: 10.1190/1.3485765.
Dollar, H., 2005, Iterative linear algebra for constrained optimization: Ph.D. thesis, University of Oxford.
Farnebäck, G., J. Rydell, T. Ebbers, M. Andersson, and H. Knutsson, 2007, Efficient computation of the inverse gradient on irregular domains: IEEE 11th International Conference on Computer Vision, IEEE, 2710–2717.
Fehmers, G. C., and C. F. Höcker, 2003, Fast structural interpretation with structure-oriented filtering: Geophysics, **68**, 1286–1293, doi: 10.1190/1.1598121.
Fomel, S., 2010, Predictive painting of 3D seismic volumes: Geophysics, **75**, no. 4, A25–A30, doi: 10.1190/1.3453847.
Fomel, S., and J. F. Claerbout, 2003, Multidimensional recursive filter preconditioning in geophysical estimation problems: Geophysics, **68**, 577–588, doi: 10.1190/1.1567228.
Gould, N. I. M., M. E. Hribar, and J. Nocedal, 2001, On the solution of equality constrained quadratic programming problems arising in optimization: SIAM Journal on Scientific Computing, **23**, 1376–1395, doi: 10.1137/S1064827598345667.
Hale, D., 2009, Structure-oriented smoothing and semblance: Center for Wave Phenomena, Report CWP-635.
Hale, D., 2013, Methods to compute fault images, extract fault surfaces, and estimate fault throws from 3D seismic images: Geophysics, **78**, no. 2, O33–O43, doi: 10.1190/geo2012-0331.1.
Harlan, W. S., 1995, Regularization by model reparameterization: http://www.billharlan.com/papers/regularization.pdf, accesses 22 June 1997.
Karimi, P., and S. Fomel, 2011, Stratigraphic coordinate system: 81st Annual International Meeting, SEG, Expanded Abstracts, 960–964.
Lomask, J. M., J. M. Francis, W. S. Kowalik, and Y. Altobi, 2011, System and method for perturbing an initial horizon-picking solution to follow local features of a volume: U.S. Patent application 13/193,300.
Lomask, J., A. Guitton, S. Fomel, J. Claerbout, and A. A. Valenciano, 2006, Flattening without picking: Geophysics, **71**, no. 4, P13–P20, doi: 10.1190/1.2210848.
Luo, S., and D. Hale, 2012, Unfaulting and unfolding 3D seismic images: Center for Wave Phenomena, Report CWP-722.
Nash, S. G., and A. Sofer, 1996, Preconditioning reduced matrices: SIAM Journal on Matrix Analysis and Applications, **17**, 47–68, doi: 10.1137/S0895479893245371.
Parks, D., 2010, Seismic image flattening as a linear inverse problem: M.S. thesis, Colorado School of Mines.
Posamentier, H., R. Davies, J. Cartwright, and L. Wood, 2007, Seismic geomorphology — An overview: Geological Society of London Special Publication, **277**, 1–14, doi: 10.1144/GSL.SP.2007.277.01.01.
Qayyum, F., P. de Groot, and N. Hemstra, 2012, Using 3D Wheeler diagrams in seismic interpretation — The HorizonCube method: First Break, **30**, 103–109.
Saad, Y., 1996, Iterative methods for sparse linear systems: PWS Publishing Company.
Stark, T. J., 2003, Unwrapping instantaneous phase to generate a relative geologic time volume: 73rd Annual International Meeting, SEG, Expanded Abstracts, 1707–1710.
Stark, T. J., 2004, Relative geologic time (age) volumes — Relating every seismic sample to a geologically reasonable horizon: The Leading Edge, **23**, 928–932, doi: 10.1190/1.1803505.
Stark, T. J., 2005, Generating a seismic Wheeler volume: 75th Annual International Meeting, SEG, Expanded Abstracts, 782–785.
Vail, P. R., R. G. Todd, and J. B. Sangree, 1977, Seismic stratigraphy and global changes of sea level — Part 5. Chronostratigraphic significance of seismic reflections: Section 2 — Application of seismic reflection configuration to stratigraphic interpretation, *in* C. E. Payton, ed., Seismic Stratigraphy — Applications to Hydrocarbon Exploration: AAPG Memoir 26, 99–116.
VanDecar, J. C., and R. Snieder, 1994, Obtaining smooth solutions to large, linear, inverse problems: Geophysics, **59**, 818–829, doi: 10.1190/1.1443640.
Van Vliet, L. J., and P. W. Verbeek, 1995, Estimators for orientation and anisotropy in digitized images: ASCI'95, Proceedings of the First Conference of the Advanced School for Computing and Imaging, 16–18.
Wu, X., and G. Zhong, 2012a, A method for generating a seismic Wheeler volume via a relative geologic time volume: 82nd Annual International Meeting, SEG, Expanded Abstracts, doi: 10.1190/segam2012-1177.1.
Wu, X., and G. Zhong, 2012b, Generating a relative geologic time volume by 3D graph-cut phase unwrapping method with horizon and unconformity constraints: Geophysics, **77**, no. 4, O21–O34, doi: 10.1190/geo2011-0351.1.
Zeng, H., M. M. Backus, K. T. Barrow, and N. Tyler, 1998a, Stratal slicing; Part 1, Realistic 3D seismic model: Geophysics, **63**, 502–513, doi: 10.1190/1.1444351.
Zeng, H., S. C. Henry, and J. P. Riola, 1998b, Strata slicing: Part II. Real 3D seismic data: Geophysics, **63**, 514–522, doi: 10.1190/1.1444352.